



# JWST/NIRCam Probes Young Star Clusters in the Reionization Era Sunrise Arc

Eros Vanzella<sup>1</sup>, Adélaïde Claeysens<sup>2</sup>, Brian Welch<sup>3,4,5</sup>, Angela Adamo<sup>2</sup>, Dan Coe<sup>6,7,8</sup>, Jose M. Diego<sup>9</sup>, Guillaume Mahler<sup>10,11</sup>, Gourav Khullar<sup>12</sup>, Vasily Kokorev<sup>13</sup>, Masamune Oguri<sup>14,15</sup>, Swara Ravindranath<sup>6</sup>, Lukas J. Furtak<sup>16</sup>, Tiger Yu-Yang Hsiao<sup>8</sup>, Abdurro'uf<sup>6,8</sup>, Nir Mandelker<sup>17</sup>, Gabriel Brammer<sup>18,19</sup>, Larry D. Bradley<sup>6</sup>, Maruša Bradac<sup>20,21</sup>, Christopher J. Conselice<sup>22</sup>, Pratika Dayal<sup>13</sup>, Mario Nonino<sup>23</sup>, Felipe Andrade-Santos<sup>24,25</sup>, Rogier A. Windhorst<sup>26</sup>, Nor Pirzkal<sup>6</sup>, Keren Sharon<sup>27</sup>, S. E. de Mink<sup>28,29</sup>, Seiji Fujimoto<sup>18,19,30,32</sup>, Adi Zitrin<sup>16</sup>, Jan J. Eldridge<sup>31</sup>, and Colin Norman<sup>6,8</sup>

<sup>1</sup> INAF—OAS, Osservatorio di Astrofisica e Scienza dello Spazio di Bologna, via Gobetti 93/3, I-40129 Bologna, Italy; [eros.vanzella@inaf.it](mailto:eros.vanzella@inaf.it)

<sup>2</sup> Department of Astronomy, Oskar Klein Centre, Stockholm University, AlbaNova University Centre, SE-106 91 Stockholm, Sweden

<sup>3</sup> Department of Astronomy, University of Maryland, College Park, MD 20742, USA

<sup>4</sup> Observational Cosmology Lab, NASA Goddard Space Flight Center, Greenbelt, MD 20771, USA

<sup>5</sup> Center for Research and Exploration in Space Science and Technology, NASA/GSFC, Greenbelt, MD 20771, USA

<sup>6</sup> Space Telescope Science Institute (STScI), 3700 San Martin Drive, Baltimore, MD 21218, USA

<sup>7</sup> Association of Universities for Research in Astronomy (AURA), Inc. for the European Space Agency (ESA), USA

<sup>8</sup> Center for Astrophysical Sciences, Department of Physics and Astronomy, The Johns Hopkins University, 3400 North Charles Street, Baltimore, MD 21218, USA

<sup>9</sup> Instituto de Física de Cantabria (CSIC-UC). Avda. Los Castros s/n. E-39005 Santander, Spain

<sup>10</sup> Institute for Computational Cosmology, Durham University, South Road, Durham DH1 3LE, UK

<sup>11</sup> Centre for Extragalactic Astronomy, Durham University, South Road, Durham DH1 3LE, UK

<sup>12</sup> Department of Physics and Astronomy and PITT PACC, University of Pittsburgh, Pittsburgh, PA 15260, USA

<sup>13</sup> Kapteyn Astronomical Institute, University of Groningen, PO Box 800, 9700 AV Groningen, The Netherlands

<sup>14</sup> Center for Frontier Science, Chiba University, 1-33 Yayoi-cho, Inage-ku, Chiba 263-8522, Japan

<sup>15</sup> Department of Physics, Graduate School of Science, Chiba University, 1-33 Yayoi-Cho, Inage-Ku, Chiba 263-8522, Japan

<sup>16</sup> Physics Department, Ben-Gurion University of the Negev, PO Box 653, Be'er-Sheva 84105, Israel

<sup>17</sup> Centre for Astrophysics and Planetary Science, Racah Institute of Physics, The Hebrew University, Jerusalem, 91904, Israel

<sup>18</sup> Cosmic Dawn Center (DAWN), Copenhagen, Denmark

<sup>19</sup> Niels Bohr Institute, University of Copenhagen, Jagtvej 128, Copenhagen, Denmark

<sup>20</sup> Department of Mathematics and Physics, University of Ljubljana, Jadranska ulica 19, SI-1000 Ljubljana, Slovenia

<sup>21</sup> Department of Physics and Astronomy, University of California, Davis, 1 Shields Avenue, Davis, CA 95616, USA

<sup>22</sup> Jodrell Bank Centre for Astrophysics, University of Manchester, Oxford Road, Manchester UK

<sup>23</sup> INAF—Trieste Astronomical Observatory, Via Bazzoni 2, I-34124, Trieste, Italy

<sup>24</sup> Department of Liberal Arts and Sciences, Berklee College of Music, 7 Haviland Street, Boston, MA 02215, USA

<sup>25</sup> Center for Astrophysics | Harvard & Smithsonian, 60 Garden Street, Cambridge, MA 02138, USA

<sup>26</sup> School of Earth and Space Exploration, Arizona State University, Tempe, AZ 85287-1404, USA

<sup>27</sup> Department of Astronomy, University of Michigan, 1085 South University Avenue, Ann Arbor, MI 48109, USA

<sup>28</sup> Max Planck Institute for Astrophysics, Karl-Schwarzschild-Strasse 1, D-85748 Garching, Germany

<sup>29</sup> Anton Pannekoek Institute for Astronomy, University of Amsterdam, Science Park 904, 1098XH Amsterdam, The Netherlands

<sup>30</sup> Department of Astronomy, The University of Texas at Austin, Austin, TX 78712, USA

<sup>31</sup> Department of Physics, University of Auckland, Private Bag 92019, Auckland, New Zealand

Received 2022 November 16; revised 2023 January 9; accepted 2023 January 12; published 2023 March 7

## Abstract

Star cluster formation in the early universe and its contribution to reionization remains largely unconstrained to date. Here we present JWST/NIRCam imaging of the most highly magnified galaxy known at  $z \sim 6$ , the Sunrise arc. We identify six young massive star clusters (YMCs) with measured radii spanning from  $\sim 20$  down to  $\sim 1$  pc (corrected for lensing magnification), estimated stellar masses of  $\sim 10^{6-7} M_{\odot}$ , and ages of 1–30 Myr based on SED fitting to photometry measured in eight filters extending to rest frame 7000 Å. The resulting stellar mass surface densities are higher than  $1000 M_{\odot} \text{pc}^{-2}$  (up to a few  $10^5 M_{\odot} \text{pc}^{-2}$ ), and their inferred dynamical ages qualify the majority of these systems as gravitationally bound stellar clusters. The star cluster ages map the progression of star formation along the arc, with two evolved systems ( $\gtrsim 10$  Myr old) followed by very young clusters. The youngest stellar clusters ( $< 5$  Myr) show evidence of prominent  $\text{H}\beta + [\text{O III}]$  emission based on photometry with equivalent widths larger than  $> 1000$  Å rest frame and are hosted in a 200 pc sized star-forming complex. Such a region dominates the ionizing photon production with a high efficiency  $\log(\xi_{\text{ion}} [\text{Hz erg}^{-1}]) \sim 25.7$ . A significant fraction of the recently formed stellar mass of the galaxy (10%–30%) occurred in these YMCs. We speculate that such sources of ionizing radiation boost the ionizing photon production efficiency, which eventually carves ionized channels that might favor the escape of Lyman continuum radiation. The survival of some of the clusters would make them the progenitors of massive and relatively metal-poor globular clusters in the local universe.

<sup>32</sup> Hubble Fellow.

*Unified Astronomy Thesaurus concepts:* [High-redshift galaxies \(734\)](#); [Young star clusters \(1833\)](#); [Reionization \(1383\)](#); [Globular star clusters \(656\)](#)

## 1. Introduction

Pioneering works in the pre–James Webb Space Telescope (JWST) era have already reported on the detection of tiny star-forming regions at cosmological distances by combining Hubble Space Telescope (HST) imaging and gravitational lensing (e.g., Ellis et al. 2001) that have only recently been recognized as globular cluster precursor (GCP) candidates (Vanzella et al. 2017, 2019; see also Elmegreen et al. 2021; Welch et al. 2023), along with the use of deep Very Large Telescope (VLT) Multi Unit Spectroscopic Explorer (MUSE) spectroscopy performed on the Hubble Frontier Fields (e.g., Vanzella et al. 2021) or exploiting superlensed arcs like the Sunburst (Rigby et al. 2017; Rivera-Thorsen et al. 2019; Sharon et al. 2022; Vanzella et al. 2022a).

Recently, exquisite JWST/NIRCam and NIRISS imaging of lensed fields at an unprecedented space-based angular resolution of 40–140 mas spanning 1–5  $\mu\text{m}$  have revealed compact sources with physical properties resembling dense stellar clusters observed locally by, e.g., Adamo et al. (2020a). In particular, such instrumental advances led to the discovery of  $z \simeq 1.37$  star clusters with evolved ages of 0.1–4 Gyr (Mowla et al. 2022; Claessens et al. 2023) in a galaxy dubbed the “Sparkler,” which is lensed by cluster SMACS 0723, observed during the JWST Early Release Observations (Pontoppidan et al. 2022). Relatively young protoglobular clusters at  $z \simeq 4$  with estimated ages of  $< 30$  Myr have also been identified in highly magnified galaxies by the A2744 galaxy cluster (Vanzella et al. 2022b) observed during the ERS-GLASS campaign (JWST program 1342, PI: T. Treu; Treu et al. 2022).

Such early results demonstrate that whenever the angular resolution increases, either by technological advancements or by means of gravitational lensing, the hierarchical organization of star formation promptly emerges (e.g., Johnson et al. 2017; Meštrić et al. 2022) showing its fundamental units: the stellar clusters. Such young stellar clusters significantly alter the properties of the interstellar medium (ISM) of the hosting galaxy during their formation phase by injecting radiative and mechanical feedback into the ISM (e.g., Heckman et al. 2011; Bik et al. 2018; Sirressi et al. 2022). These are also key processes that might efficiently carve ionized channels and favor the escape of ionizing photons (e.g., James et al. 2016; Micheva et al. 2017; Rivera-Thorsen et al. 2019; Vanzella et al. 2022a).

In this work, we report on JWST/NIRCam observations of the Sunrise arc, the most highly magnified galaxy known at  $z \sim 6$  (Salmon et al. 2020; Welch et al. 2023) and host to the lensed star Earendel (Welch et al. 2022a, 2022b). Welch et al. (2023) analyzed the star-forming regions of the galaxy based on HST imaging. Here we use JWST to further characterize the same regions which—despite the very large lensing amplification—appear rather nucleated and/or barely resolved, making them some of the best candidates for GCPs.

Throughout this paper, we assume a flat cosmology with  $\Omega_M = 0.3$ ,  $\Omega_\Lambda = 0.7$ , and  $H_0 = 70 \text{ km s}^{-1} \text{ Mpc}^{-1}$ . For this model,  $1'' = 6.50 \text{ kpc}$  at the redshift of the cluster ( $z = 0.566$ ), and  $1'' = 5.61 \text{ kpc}$  for a source at the redshift of the Sunrise arc ( $z = 6.2$ ). All magnitudes are given in the AB system (Oke & Gunn 1983):  $m_{\text{AB}} = 23.9 - 2.5 \log(f_\nu / \mu\text{Jy})$ . In this work, we use the terms star-forming “clumps” or “knots” as synonyms when

referring to a subcomponent of an existing galaxy, keeping in mind that the star-forming knot operational definition often applies to a source that appears nucleated or compact. With the term “stellar clusters,” we refer to the usual definition of local gravitationally bound young (massive) star clusters (Gieles & Portegies Zwart 2011) having a large dynamical age, high stellar mass surface density  $\Sigma_M \gtrsim 1000 M_\odot \text{ pc}^{-2}$ , and radii  $\lesssim 30 \text{ pc}$  (see Section 3.3). Depending on the available angular resolution, a clump or knot can be a star-forming complex or a single stellar cluster, as discussed in this work.

All data analyzed in this paper are publicly available. We provide data products and analysis notebooks at our website.<sup>33</sup>

## 2. JWST and HST Imaging

The massive galaxy cluster WHL J013719.8082841 ( $z = 0.566$ ; Wen et al. 2012; Wen & Han 2015) was observed by the Reionization Lensing Cluster Survey (HST GO program 14096; Coe et al. 2019) and two follow-up HST GO programs, 15842 and 16668 (PI: Coe). These data have recently been reprocessed and included in the CHaRGE archive (Kokorev et al. 2022).

The JWST/NIRCam observations were acquired on 2022 July 30 (Bradley et al. 2022; Welch et al. 2022b). Briefly, the cluster was observed in eight filters covering the spectral range from 0.8 to 5  $\mu\text{m}$  (F090W, F115W, F150W, F200W, F277W, F356W, F410M, and F444W) with an integration time of 2104 s each. The superb angular resolution of JWST/NIRCam provided point-spread functions (PSFs) with FWHM values ranging from  $0''.04$  to  $0''.14$  from 1 to 5  $\mu\text{m}$ , respectively. Such values were verified on a selected sample of nonsaturated or uncontaminated stars identified in the same field.

We use the GRIZLI pipeline (Brammer et al. 2022) to process all HST and JWST individual calibrated exposures (FLT and level 2b CAL images, respectively). We coadd all exposures in each filter and align them to a common  $0''.04 \text{ pixel}^{-1}$  grid with coordinates registered to the Gaia DR3 catalogs (Gaia Collaboration et al. 2021). We drizzle the NIRCam short-wavelength images (F090W, F115W, F150W, and F200W) to higher resolution,  $0''.02 \text{ pixel}^{-1}$ . The GRIZLI v4 data products are publicly available.<sup>34</sup> In our analysis, we use the NIRCam calibrations `jwst_0995.pmap`, based on analysis of NIRCam CAL program data and made operational on 2022 October 6.

### 2.1. A Supermagnified Arc at $z = 6.0$ and the Emergence of Tiny Star-forming Regions

Thanks to the extended wavelength coverage produced by the NIRCam data, we have refined the redshift estimate of the Sunrise arc. Appendix A presents the spectral energy distribution (SED) fitting of the host multiband photometry (see Section 4.1), which results in a redshift probability distribution narrowly peaked at  $z = 6.0 \pm 0.2$  (95% CL), with no significant likelihood at other redshifts. This is fully consistent with previous estimates based on HST imaging (Salmon et al. 2020; Welch et al. 2023). In the following, we adopt the fiducial value of  $z = 6.0$  as the current best solution for the

<sup>33</sup> <http://cosmic-spring.github.io>; <https://github.com/cosmic-spring/Sunrise-Arc>

<sup>34</sup> <https://s3.amazonaws.com/grizli-v2/JwstMosaics/v4/index.html>

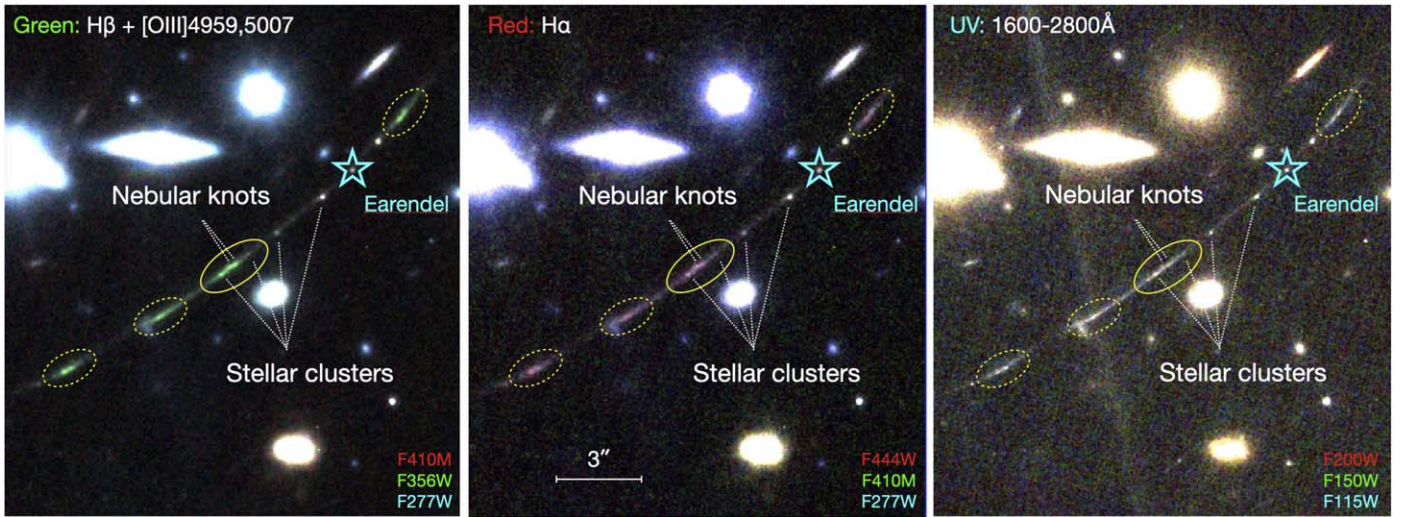


**Figure 1.** The JWST/NIRCam color composites of the Sunrise arc. The RGB images highlight the  $H\beta + [O\text{ III}]$  (left; green channel),  $H\alpha$  (middle; red channel), and ultraviolet continuum  $\sim 1600\text{--}2800\text{\AA}$  along the entire arc (right). The YMCs and the nebular knots are indicated with dotted lines. In the bottom right corner of each panel, we report the set of filters used to build the color images. Ellipses mark the four multiple images of the star-forming complex (dubbed SFC in the text). In the right panel, it is visible as a diffraction spike that intercepts the region labeled 6c (see text and Figure 2). Such a region is not considered in this work.

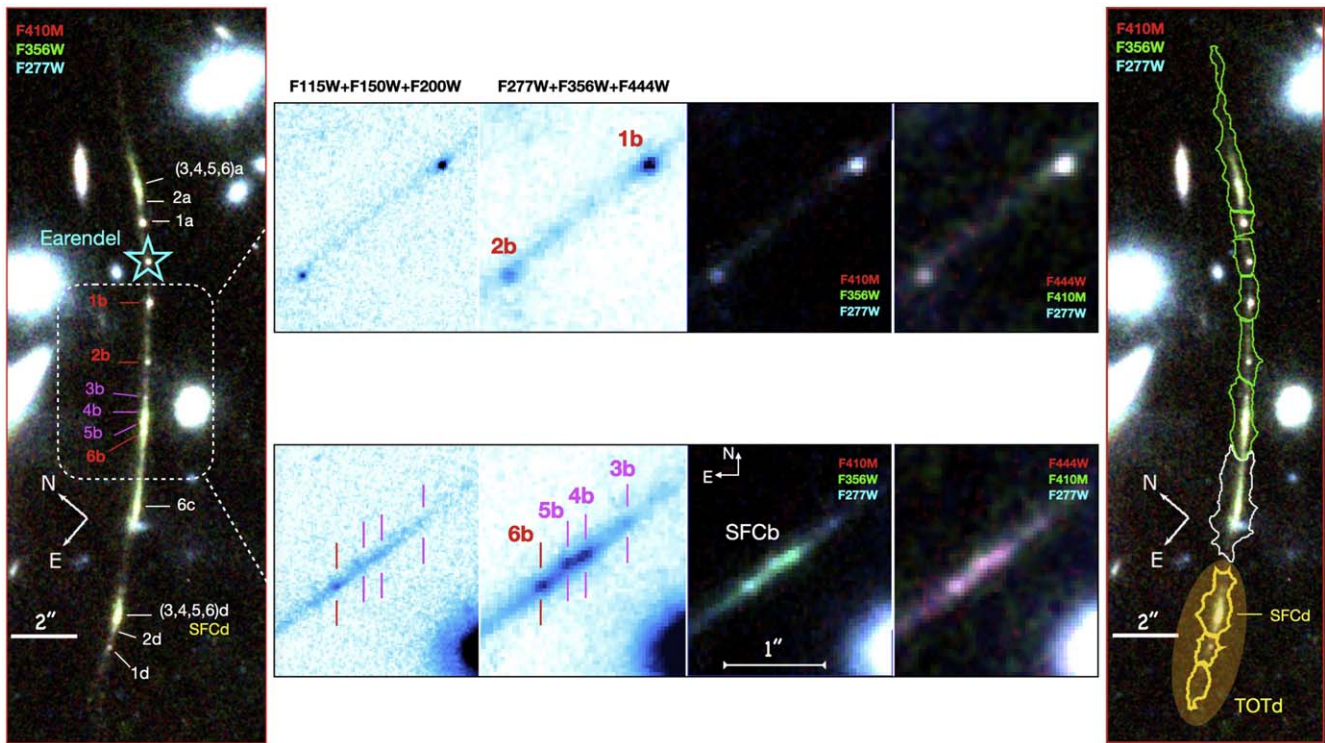
Sunrise arc (upcoming NIRSpectroscopy will provide definitive estimates). The results presented in this work remain the same within the uncertainties of the redshift estimate.

Figure 1 shows the JWST/NIRCam color images of the Sunrise arc along with the identified star-forming regions, as well as the star (or star system) Earendel. The arc extends  $\sim 17''$  along the tangential direction and includes multiple images of a set of tiny knots. The total magnification is  $\mu \sim 300$  based on HST-derived lens models (Welch et al. 2023). After minor updates to the lens models based on JWST imaging as described in Appendix B, we find large tangential (linear) magnifications of  $(30\text{--}70)\times$  for individual knots. Such a tangential stretch corresponds to  $2\text{--}4\text{ pc pixel}^{-1}$  (adopting  $20\text{ mas pixel}^{-1}$ ) at  $z \simeq 6.0$ . The presence of barely resolved and unresolved sources despite the very large magnification implies that their intrinsic sizes are very small (as observed in other systems; e.g., Johnson et al. 2017; Rigby et al. 2017; Vanzella et al. 2019; Bouwens et al. 2021). Small effective radii of the sources were already estimated based on HST imaging with upper limits as small as 3 pc for unresolved sources (Welch et al. 2023). The unmatched angular resolution ( $< 80\text{ mas}$  at  $\lambda < 2\text{ }\mu\text{m}$ ) and unique wavelength coverage (up to  $5\text{ }\mu\text{m}$ ) provided by JWST/NIRCam allow us to spatially resolve all of the previously identified clumps and measure radii as small as  $\sim 1\text{ pc}$ .

Six relatively compact knots have been visually identified after inspecting all of the JWST/NIRCam bands. Figure 2 shows multiple images of the Sunrise (labeled as “a,” “b,” “c,” and “d”) with the associated knots ranging from 1 to 6. In particular, objects 1b, 2b, and 6b appear in all bands, from the rest-frame ultraviolet stellar continuum ( $1600\text{--}2800\text{ \AA}$ ) to the optical  $7000\text{ \AA}$ ; see Figure 1. The same Figure 1 also shows a diffraction spike that intercepts the region labeled 6c. While such a spike does not significantly affect the photometry in that region, 6c is not used in the rest of the work. These clumps are also clearly detected in the HST data. However, knots 3b, 4b, and 5b emerge only in the redder NIRCam bands, F277W, F356W, and F444W. In the low-resolution HST data, object 3b is undetected, while 4b and 5b appear as a single clump. As

discussed in the next section, we refer to these three as “nebular” knots, as we find that the photometry in the aforementioned bands could be boosted by nebular  $[O\text{ II}] \lambda 3727, 3729, H\beta + [O\text{ III}] \lambda \lambda 4959, 5007$ , and  $H\alpha$  emission, respectively. These nebular knots do not show a clear compact emission in the rest-frame ultraviolet-stacked image (F115W, F150W, and F200W; see Figure 2).

The identification of high- $z$  sources in the lensed fields depends on several effects (sizes, magnitudes, magnification, etc.) and requires dedicated simulations and/or a forward-modeling approach (e.g., Plazas et al. 2019; Bergamini et al. 2022; Bouwens et al. 2022). We briefly address here the completeness in detecting compact sources ( $< 10\text{ pc}$ ) in the Sunrise arc, while we postpone a full analysis to the near future when upcoming MUSE and NIRSpectroscopy will enable us to derive a more robust lensing model for this galaxy cluster. Stellar clusters with sizes smaller than  $10\text{ pc}$  appear as (or nearly as) pointlike sources in the lens plane in the very magnified regime studied here. The  $2\sigma$  limits of JWST/NIRCam imaging for pointlike sources in the F150W (ultraviolet rest frame) and F410M (optical rest frame) bands are  $29.5$  and  $29.6\text{ mag}$ , respectively (Bradley et al. 2022), which correspond to  $> 33.2$  and  $> 33.3$  adopting  $\mu_{\text{tot}} > 30$  (the expected lower value along the most magnified portion of the arc; see Appendix B). The absolute magnitudes associated with these limits are  $> -13.5$  and  $> -13.6\text{ mag}$  (they become  $\sim 0.5\text{ mag}$  fainter if  $\mu_{\text{tot}} = 50$ ). Such luminosities correspond to different stellar masses of the star clusters, depending on the assumed initial mass function (IMF), age, metallicity, and dust extinction (in the ultraviolet). For simplicity, we consider the Starburst99 models (Leitherer et al. 2014), an instantaneous burst that is suitable for such tiny sources (see below), the Salpeter IMF, and metallicity  $Z = 0.008$ , where  $Z$  is the mass fraction of all elements heavier than helium (though the results do not depend significantly on  $Z$ ). The above ultraviolet absolute magnitude limit corresponds to a  $10^6 M_{\odot}$  star cluster at  $40\text{ Myr}$ , or  $0.2 \times 10^6 M_{\odot}$  at  $10\text{ Myr}$ . Given the depth of the NIRCam imaging, the geometrical configuration, and the high magnification regime of the Sunrise arc, we are likely



**Figure 2.** Summary of the detected clumps. In the left panel, the Sunrise arc is shown in the color-composite JWST/NIRCam image in filters F277W (blue), F356W (green), and F410M (red), with labels indicating the clumps discussed in this work. Group “b” represents the most magnified ones, whereas the other multiple images are indicated with white labels. Within group “b” (dotted square), the red labels mark the knots identified in the ultraviolet continuum (F115W, F150W, and F200W), whereas the magenta ones mark the nebular knots not detected in the ultraviolet but that emerge where the optical nebular lines are expected to lie (F277W, F356W, and F444W; see text for more details). The middle panels show the thumbnails of stacked JWST/NIRCam bands (F115W+F150W+F200W) and (F277W+F356W+F444W). The same colored labels shown in the left panel are reported in the middle panels. The color-composite images highlight the absence/presence of optical nebular emission lines (see also Figure 1). In the right panel, the map of segments discussed in Section 4.1 is shown in the same color image as shown on the left. Regarding the extended regions, in this work, we make use of the segments dubbed SFCd (indicated with the corresponding label) and TOTd (marked with a transparent yellow ellipse) and the combination of all segments except the white one for the estimation of the photometric redshift (Appendix A).

recovering all young star clusters with stellar masses  $> 0.5 \times 10^6 M_{\odot}$  at ages younger than 10 Myr and more massive than  $10^6 M_{\odot}$  up to ages of 40 Myr.

### 3. Physical Properties of Stellar Cluster Candidates

#### 3.1. Photometry and Size Estimates

The fluxes and sizes of each star cluster candidate/knot are obtained by adopting the methodology presented in Claeysens et al. (2023), following Messa et al. (2022).

Different from clump photometric analyses based on fixed aperture photometry (e.g., Mowla et al. 2022), we account for the shape of the clump while measuring fluxes. We simultaneously fit for both quantities with a grid of models that are the resulting convolution of a 2D Gaussian profile<sup>35</sup> with the measured PSF model in the image plane. The PSF is built in each JWST filter by selecting and stacking observed stars in the frame. A local background gradient (i.e., emission from the galaxy light) is also fitted and removed. Since not all of the clusters/knots are visible in the far-UV, we use the NIRCam F150W image to determine the intrinsic shape ( $x_{\text{std}}$ ,  $\epsilon$ ,  $\theta$ ) of star cluster candidates 1b, 2b, and 6b using a  $9 \times 9$  pixel box centered on the source. For nebular knots 3b, 4b, and 5b, we use the NIRCam F277W image as the reference filter to

measure their sizes. Due to their proximity, 4b and 5b are fitted simultaneously. Figure 3 shows the residuals after subtracting the models from the NIRCam images. Once the intrinsic shape of the object is determined, we derive the fluxes in the other filters by fixing the 2D Gaussian shape ( $x_{\text{std}}$ ,  $\epsilon$ , and  $\theta$  values), convolving it with the filter PSF, and letting the center of the Gaussian, the normalization (i.e., the integrated flux), and the local background be free parameters. We fit the shape of the source and the underlying background within the  $9 \times 9$  pixel box. The total flux of the source is obtained by extrapolating to infinite the best-fit 2D Gaussian shape. The final photometric errors include in quadrature the Poissonian error, as well as the uncertainties in the measured parameters of the shape (for more details, see Claeysens et al. 2023). The latter error is significantly larger in the nebular knots (see Figure 4), which are not well detected in the continuum bands.

The intrinsic effective radius  $R_{\text{eff}}$  of each source is derived in the reference frame (F150W for 1b, 2b, and 6b and F277W for 3b, 4b, and 5b) by converting the  $x$  and  $y$  standard deviations of the 2D Gaussian into a circular radius, applying the multiplicative factor to get the FWHM, and then determining  $R_{\text{eff}}$  as half of the FWHM. These values are reported in parsecs and observed angular scale in Table 3 after distance and tangential magnification have been taken into account. In particular, the inferred angular size in the lens plane is divided by  $\mu_{\text{tang}}$  and converted into parsecs. The magnitudes of each clump are reported in Table 1.

<sup>35</sup> The 2D Gaussian profile is parameterized by the clump position ( $x_0$  and  $y_0$ ), minor axis standard deviation ( $x_{\text{std}}$ ), ellipticity ( $\epsilon$ ), positional angle ( $\theta$ , describing the orientation of the ellipses), and flux ( $f$ ).

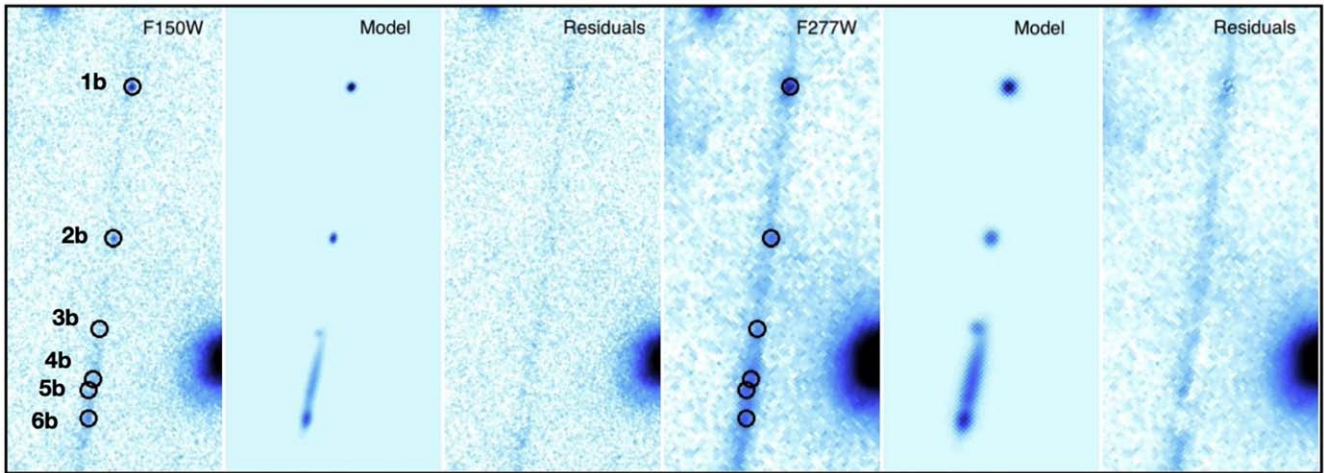


**Figure 3.** The resulting fitted shapes (models) and residuals are shown for the knots of group “b” reported in Table 3. The sizes of 1b, 2b, and 6b are derived from image F150W, while the nebular knots 3b, 4b, and 5b are from image F277W.

### 3.2. SED Fitting Analysis of Star Cluster Candidates

The SED fitting analysis has been performed following the methodology described in Claeysens et al. (2023).

Motivated by the small physical scales probed ( $\lesssim 10$  pc), which easily overlap with star-forming regions and star cluster sizes in the local universe, we fit with the single stellar population models of Yggdrasil (Zackrisson et al. 2011). These models include a full self-consistent treatment of ionized gas emission using Cloudy (Ferland et al. 1998) with a fully populated Kroupa (2001) IMF. The model spectra have been redshifted to  $z = 6.0$ , and Calzetti et al. (2000) dust attenuation has been applied. We adopted two different metallicities,  $Z = 0.004$  and  $0.0004$  (corresponding to about 30% and 3% of the solar metallicity as determined by Asplund et al. 2009), finding that both fit the observed SEDs similarly well (Figure 4). It is known that optical SED rest frames are not very sensitive to metallicity; therefore, in Table 3, we report the best solutions using models with 30% solar abundances, but we also include the best-fit model with 3% solar metallicity in Figure 4. We note that the solutions determined with 3% solar metallicity yield physical parameters in agreement within the uncertainties. The associated uncertainties have been derived using the 68% distributions recovered by fitting 100 realizations of the observed SEDs after photometric uncertainties have been propagated using Monte Carlo sampling.

Four of the six compact cluster candidates, 3b, 4b, 5b, and 6b, have clear photometric jumps in the broad bands containing strong emission lines, which imply large equivalent widths of the optical nebular lines. Conversely, sources 1b and 2b do not show such a prominent nebular emission in the photometric SEDs, implying a smaller ionization field and more evolved stellar populations. The modeling of the SEDs shown in Figures 4 and 5 illustrates this behavior. The resulting ages reported in Table 3 confirm the expectations. The ages of the clusters become progressively younger along the arc, from 30 down to 1 Myr. Recovered masses are all above  $10^6 M_{\odot}$ , in agreement with the completeness limits for point sources described above.

### 3.3. YMCs Populating the Sunrise Galaxy

The very small sizes ( $< 10$  pc) and large stellar mass surface densities ( $> 1000 M_{\odot} \text{ pc}^{-2}$ ) are fully consistent with those

observed in young massive star clusters (YMCs;  $> 10^5 M_{\odot}$ ; e.g., Brown & Gnedin 2021) and globular clusters (e.g., Norris et al. 2014) in the local universe. Furthermore, the inferred dynamical age  $\Pi$ , defined as  $\Pi = \text{age}/T_{\text{CR}}$  (where  $T_{\text{CR}}$  is the crossing time; Gieles & Portegies Zwart 2011; Adamo et al. 2020a),<sup>36</sup> implies that the majority of the sources are gravitationally bound stellar clusters ( $\Pi > 1$ ; see Table 3). Two of them, 1b and 2b, appear relatively evolved (with no evidence of detectable ionized gas emission in their observed SEDs; Figure 4), with ages spanning the range  $\simeq 10$ –30 Myr and  $\Pi \gg 1$ . Remarkably, both of them show properties reminiscent of local massive globular clusters (see Section 5.1). On the other hand, cluster candidate 6b is in the bursty formation phase with an age of  $< 5$  Myr and still appears as a bound young star cluster (although note that the  $\Pi$  at such young ages is ill-defined, with the crossing time comparable to the age of the system), in which the strong ionization field provided by hot stars pumps significantly large optical emission lines (see Section 5.2).

It is worth noting the presence of three additional knots (3b, 4b, and 5b) that are clearly visible in the F277W, F356W, and F444W bands only, without any clear yet compact counterpart in the stacked image (F115W + F150W + F200W), that cover the rest-UV continuum (see Figure 2). Interestingly, the bands where the sources are detected include the [O II], H $\beta$ + [O III], and H $\alpha$  lines, respectively. For this reason, we refer to them as “nebular-dominated knots.” The sizes of these nebular knots have been inferred from the F277W band, which provides the sharpest PSF (among the three mentioned above), and are remarkably small, with effective radii spanning the interval  $R_{\text{eff}} = 4$ –25 pc (although these values have large uncertainties). Under the assumption that such rest-frame optical high-ionization lines, like [O III], trace the location of hot stars (as observed in the local universe; e.g., James et al. 2016; Sirressi et al. 2022), it is plausible that these detected compact nebular emissions host stellar clusters. Their SED analysis suggests that these are hidden clusters. They have significant dust attenuation

<sup>36</sup> The  $\Pi$  has been extensively used to identify bound star clusters in the local universe (e.g., Ryon et al. 2017; Adamo et al. 2020b). The crossing time expressed in megayears is defined as  $T_{\text{CR}} = 10 \times (R_{\text{eff}}^3 / GM)^{0.5}$ , where  $M$  and  $R_{\text{eff}}$  are the stellar mass and effective radius, respectively, and  $G \approx 0.0045 \text{ pc}^{-3} M_{\odot}^{-1} \text{ Myr}^{-2}$  is the gravitational constant.

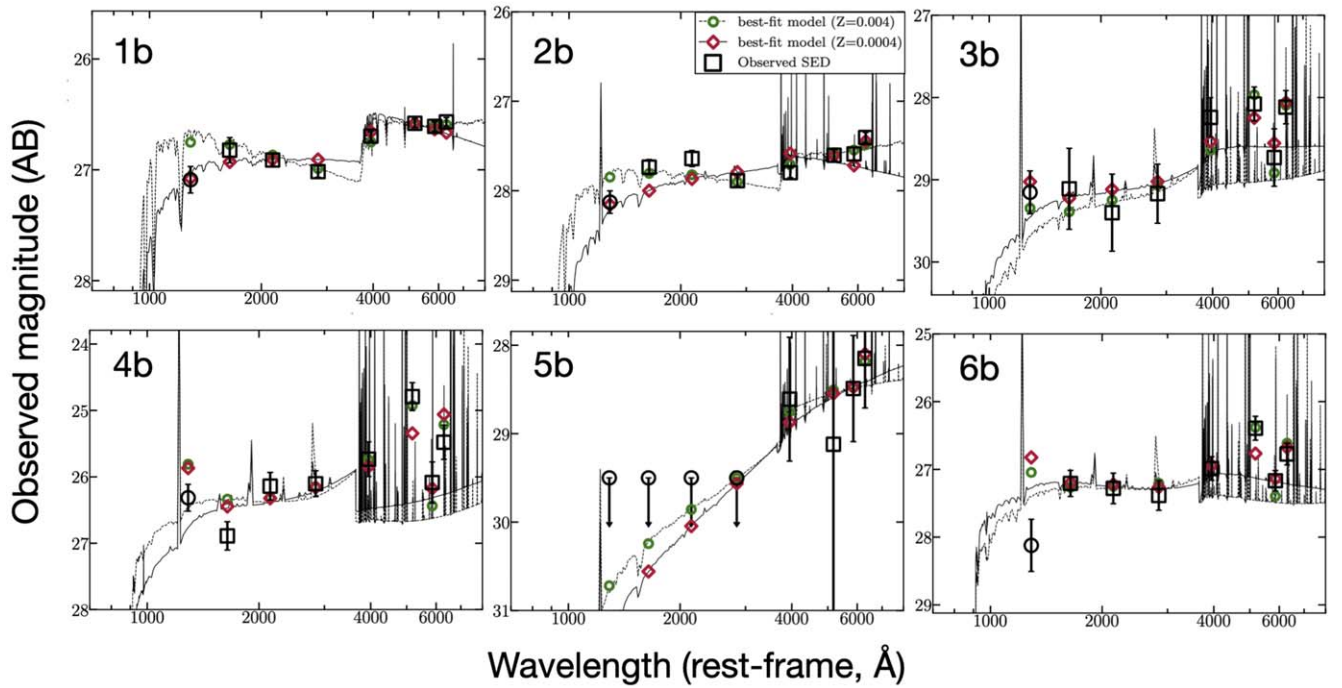


**Figure 4.** The SED analysis of the compact regions identified as stellar clusters and star-forming knots in the *Sunrise* galaxy. Sources 1b and 2b are relatively evolved dense star clusters and do not show evident rest-frame optical emission lines, while sources 3b, 4b, and 5b are barely or even not detected in the F150W+F200W+F277W stacked image (probing the ultraviolet wavelengths 1500–2500 Å) and are referred in the main text as nebular knots possibly hosting dust-obscured star clusters. The physical quantities of the SED fitting are reported in Table 3.

( $E(B - V)$  between 0.15 and 0.35 mag), which explains why we do not clearly detect them in the UV, while longer (optical rest frame) wavelengths emerge by means of prominent emission lines. This is the first evidence of star clusters still embedded in their natal formation region detected at a cosmological distance.

## 4. Physical Properties of the Extended Star-forming Complex and Host

### 4.1. Photometry of Extended Regions

We extract isophotal photometry in nine regions detected along the arc. We construct a detection image created from background-subtracted F277W, F356W, and F410M NIRCcam mosaics. The area of interest shown in Figure 2 is crowded with galaxy cluster members, background objects, and the diffuse intracluster light, which presents a challenge toward robustly segmenting our sources. To ensure consistency between our detection parameters and cover the large dynamic range of brightness of the sources in the field, we separate the detection image to cover three regions along the arc, which contain the following knots: (1) 1d, 2d, and 6d; (2) 6c, 6b, 2b, and 1b; and (3) 1a and 6a. We smooth the detection images with a median filter of `pixel_size=2`, similarly to the procedure adopted in Livermore et al. (2017) and Kokorev et al. (2022). Finally, the segmentation maps are produced by running SEP (Barbary 2016) and further smoothed with a median filter of `pixel_size=8`. The map of segments is shown in Figure 2.

We apply the final segments to all available JWST and HST mosaics, which we have matched to the F444W PSF. We also subtract the local background in each subregion containing the knots. We designed our isophotal apertures to be fairly large, so we do not perform any further aperture corrections.

Coordinates and photometry for the objects analyzed in this work are given in Table 2.

### 4.2. SED Fitting Analysis

While the star cluster candidates have been fitted with instantaneous burst models (i.e., single stellar populations), we allow for an extended period of constant and flexible star formation in fitting the SFC, appropriate for large regions of a galaxy, as well as the total flux from the host galaxy.

#### 4.2.1. BAGPIPES

We perform SED fitting with BAGPIPES (Carnall et al. 2018) in a manner similar to Hsiao et al. (2022). Briefly, we use BPASS v2.2.1 SED templates (Stanway & Eldridge 2018) reprocessed with CLOUDY c17.03 (Ferland et al. 1998, 2013, 2017). We use the fiducial BPASS IMF `imf135_300` with a high-mass slope similar to Kroupa (2002). We allow the ionization parameter  $U$  to range between  $\log(U) = -4$  and  $-1$ . For dust attenuation, we use the Salim et al. (2018) parameterization capable of reproducing Milky Way and SMC attenuation curves. Young stars (age  $< 10$  Myr) residing in stellar birth clouds experience more dust extinction by a factor  $\eta$  in the range 1–3.

For SFC, we assumed a constant star formation rate (SFR) with one or two components. The single-component result was  $\sim 2 M_{\odot} \text{ yr}^{-1}$  over  $\sim 20$  Myr after delensing (Table 3). The two-component result was  $\sim 3 M_{\odot} \text{ yr}^{-1}$  over  $\sim 10$  Myr plus a longer duration of  $\sim 0.1 M_{\odot} \text{ yr}^{-1}$  over  $\sim 600$  Myr. The long-duration SFR result is similar to the result we obtain when fitting to the extended portion of the arc with no clumps. Allowing for this longer-duration component increases our mass estimate for SFC to  $\sim 10^8 M_{\odot}$ , twice that derived when assuming a single-component constant SFR.

**Table 1**  
JWST/NIRCam Extracted Photometry of Each Star-forming Knot and/or Cluster Candidate

ID	R.A.	Decl.	F090W	F115W	F150W	F200W	F277W	F356W	F410M	F444W
(1)	(2)	(3)	(4)	(5)	(6)	(7)	(8)	(9)	(10)	(11)
1b	23.313	53.13	27.13(0.12)	26.85(0.11)	26.93(0.11)	27.03(0.1)	26.7(0.09)	26.59(0.09)	26.61(0.09)	26.57(0.09)
2b	23.413	54.29	28.17(0.13)	27.77(0.14)	27.66(0.14)	27.9(0.12)	27.81(0.11)	27.61(0.11)	27.59(0.12)	27.41(0.11)
3b	23.474	54.97	29.2(0.26)	29.14(0.49)	29.42(0.47)	29.18(0.36)	28.25(0.24)	28.08(0.21)	28.74(0.35)	28.12(0.2)
4b	23.504	55.30	26.26(0.2)	26.92(0.21)	26.16(0.21)	26.12(0.2)	25.74(0.26)	24.8(0.21)	26.09(0.31)	25.48(0.26)
5b	23.515	55.40	29.3(-)	29.4(-)	29.5(-)	29.7(-)	28.61(0.7)	29.12(2.28)	28.49(0.56)	28.15(0.67)
6b	23.533	55.63	28.17(0.38)	27.24(0.19)	27.3(0.23)	27.4(0.22)	26.99(0.17)	26.4(0.18)	27.17(0.15)	26.78(0.16)

**Note.** Magnitudes and  $1\sigma$  errors (in parentheses) are reported for the NIRCam filters. Errors denoted (-) indicate lower limits at  $2\sigma$  (Bradley et al. 2022). The method to determine these values is described in Section 3.1.

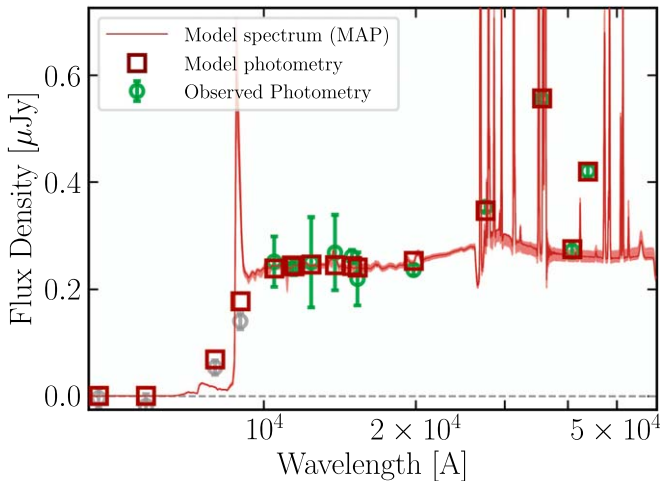


**Figure 5.** Prospector SED fit to lensed image d of the star-forming complex SFC (SFCd). The best-fit SED is shown in red, the fitted photometry is shown in green (gray points are masked photometry values), and the best-fit model photometry is depicted in brown. The physical quantities inferred from the SED fitting process are reported in Table 3.

We also explored SED fitting with 2016 version BC03 models (Bruzual & Charlot 2003), including empirical MILES stellar spectra (Falcón-Barroso et al. 2011; Vazdekis et al. 2016), similarly reprocessed with CLOUDY. These templates failed to reproduce the strong nebular emission lines inferred in SFC (see Wofford et al. 2016 for a similar result). In the BPASS models, binary interactions produce helium stars that are hotter ( $T_{\text{eff}} = 10^5$  K; see, Göteborg et al. 2018, 2019), yielding stronger O32 line ratios (Xiao et al. 2018, 2019).

#### 4.2.2. Prospector

We perform complementary SED fitting analyses of observed photometry in the star-forming complex (SFC) and the host galaxy (TOTd) with the Markov Chain Monte Carlo-based stellar population synthesis (SPS) and parameter inference code, Prospector.

Prospector is based on the Python-FSPS framework with the MILES stellar spectral library and the MIST set of isochrones (Conroy & Gunn 2010; Falcón-Barroso et al. 2011; Choi et al. 2016; Johnson et al. 2021).

In these models, we fit for a nonparametric star formation history (SFH) observed at a notional redshift  $z = 6$ . We utilize age bins with [0–20], [20–50], [50–100], [100–300], [300–600], and [600–900] Myr in lookback time, represented by the parameters  $\text{SFR}_{\text{ratio}}$ , referring to the ratio of total star

formation in adjacent time bins. The priors for the SFR ratios in adjacent time bins are ascribed to the continuity prior. These parameters fit for the change in  $\log(\text{SFR})$  between the bins and statistically prefer smooth transitions in SFR (see Leja et al. 2019).

We also fit for dust attenuation using the Kriek & Conroy (2013) attenuation law applied to all of the light from the galaxy (in units of opacity at 5500 Å) while simultaneously constraining the index of the attenuation power law. We also use as free parameters the stellar and gas-phase metallicities  $\log(Z/Z_{\odot})$  (where  $Z_{\odot} = 0.0142$ , as determined by Asplund et al. 2009, and with flat priors between  $[-2.0, 0.2]$ ), the gas ionization parameter  $U$  (with flat priors sampled between  $[-4, -1]$ , similar to the BAGPIPES analysis), and the remnant stellar mass in the galaxy ( $M_{\text{remnant}}$ , in units of  $M_{\odot}$ ). We assume a Chabrier IMF (Chabrier 2003), and intergalactic medium absorption is present in these models. Nebular continuum and line emission are used in the fit, and a nominal velocity smoothing of  $200 \text{ km s}^{-1}$  was used for the model spectrum. For more details on applying nonparametric SFH models to lensed galaxy observations that sample rest-frame UV and optical emission, refer to, e.g., Khullar et al. (2021) and Sukay et al. (2022).

We mask photometry redward of F090W in this analysis, which samples Ly $\alpha$  emission (that is not constrained without spectroscopy and is decoupled from star formation due to geometrical considerations). The observed photometry of the SFCd, the corresponding best-fit SED model, and the predicted model photometry are shown in Figure 5. We also provide the inferred parameter values—including remnant (delensed) stellar masses and mass-weighted ages—in Table 3.

#### 4.3. Mapping the SFH of the Sunrise Arc

The SFH model assumptions need to be incorporated when inferring the remnant stellar mass and age and the mass assembly in the Sunrise arc (and its constituents). After considering the uncertainties ( $\sim 0.4$  dex in both analyses), we infer a  $1.4\sigma$  difference between the BAGPIPES (constant SFH,  $\log M_{\text{median}} \sim 8.5$ ) and Prospector (flexible SFH with six age bins,  $\log M_{\text{median}} \sim 9.3$ ) stellar masses.

We attribute this difference to the modeling assumptions; e.g., Leja et al. (2019) found a difference of 0.2–0.4 dex in median values of stellar mass between inferred values from parametric versus nonparametric SFHs. For photometric fitting, this also has consequences for inferred mass-weighted ages, metallicities, and dust properties. For the total galaxy flux and SFC, our Prospector analysis results in mass-weighted ages

**Table 2**  
JWST/NIRCam Isophotal Photometry of the Extended Regions

ID (1)	F090W (2)	F115W (3)	F150W (4)	F200W (5)	F277W (6)	F356W (7)	F410M (8)	F444W (9)
SFCd	26.03(0.12)	25.44(0.07)	25.36(0.05)	25.47(0.05)	25.03(0.02)	24.54(0.01)	25.31(0.05)	24.84(0.03)
TOTd	25.54(0.10)	25.12(0.07)	25.07(0.05)	25.10(0.05)	24.68(0.02)	24.29(0.01)	24.86(0.05)	24.54(0.03)
TOT	24.28(0.06)	23.71(0.03)	23.74(0.03)	23.69(0.02)	23.26(0.01)	22.86(0.01)	23.35(0.02)	23.11(0.01)

**Note.** Magnitudes and  $1\sigma$  errors are reported in each column for the extended regions reported in Figure 2, as derived in Section 4.1. The ID = “TOT” is the photometry of the full arc (which combines the three regions marked with transparent ellipses in Figure 8), and the SFCb and TOTd are reported in Figure 2.

of  $\sim 200$  and  $\sim 140$  Myr, respectively; this is an older inferred age than the single stellar population or constant SFH modeling.

## 5. Discussion

### 5.1. Formation of Proto-Globular Clusters in the Sunrise Arc?

Since we have access to the host’s physical properties, we can provide first-order estimates of the total cluster formation efficiency (CFE) in the Sunrise galaxy (TOTd). The CFE is broadly defined in the literature as the ratio between the total mass forming in stars divided by the total stellar mass formed in the region within a given interval of time (see Krumholz et al. 2019). Following Adamo et al. (2017), the CFE is the ratio between the cluster formation rate and the SFR of the galaxy hosting the star clusters, both calculated over a comparable interval of time  $dt$  (with the cluster formation rate defined as the total stellar mass forming in the cluster over the same  $dt$ ). The BAGPIPES and Prospector analyses suggest that the galaxy has built between  $\sim 3 \times 10^8$  and  $\sim 2 \times 10^9 M_\odot$  stellar mass over the course of 200 Myr or so. If we assume these to be lower and upper mass estimates, we can compare them with the total mass in star clusters by dividing each mass estimate by their respective ages to get a first-order estimate of the SFR. The total mass in the cluster is  $3.0 \times 10^7 M_\odot$  formed over 30 Myr, resulting in an SFR of  $1 M_\odot \text{ yr}^{-1}$  for the clusters. In the case of the host, the SED fit analyses find a minimum and maximum SFR of 3 up to  $10 M_\odot \text{ yr}^{-1}$ . The ratio will result in a CFE between 10% and 30% for the entire Sunrise arc. These estimates do not account for the mass in star clusters below the detection limits, so they should be considered lower limits. It is interesting to notice that the recovered values bracket the CFE reported for the Sunburst arc at redshift 2.4 by Vanzella et al. (2022a).

The area of the segment that contains the whole host (TOTd) corresponds in physical scales to  $6.0 \pm 2.0 \text{ kpc}^2$  (adopting an error of 30% on the magnification). The total minimum and maximum SFR surface density ( $\Sigma_{\text{SFR}}$ ) are therefore 0.5 and  $1.7 M_\odot \text{ yr}^{-1} \text{ kpc}^{-2}$ . Extrapolating from the CFE versus  $\Sigma_{\text{SFR}}$  relation (e.g., Adamo et al. 2020b), we expect about 30%–60% of the star formation in the host to happen in YMCs, which is in agreement with the lower limits reported above.

These high cluster formation efficiencies are similar to those reported in the local universe for green-pea analogs at distances of  $\sim 50$  Mpc, namely, ESO 338-IG04 and SBS 0335-052E (Adamo et al. 2011). Both of these galaxies host very massive clusters ( $> 10^5 M_\odot$ ); ESO 338-IG04 harbors an  $\sim 6$  Myr old compact cluster with a measured dynamical mass of  $1.3 \times 10^7 M_\odot$  (Östlin et al. 2007), and SBS 0335-052E is among the most metal-poor ( $\sim 5\% Z_\odot$ ) galaxies in the nearby universe

(Herenz et al. 2017). It hosts six YMCs with masses well above  $10^5 M_\odot$  and ages younger than 15 Myr (Adamo et al. 2010). The physical properties of the clusters hosted by SBS 0335-052E show a very similar age spread as observed in the YMCs of the Sunrise arc. The EW( $H\alpha$ ) of the two youngest clusters in SBS 0335-052E is a few thousand angstroms, suggesting very young ages, similar to the knots embedded in the SFC complex.

Applying the conversion by Vazdekis et al. (2015)<sup>37</sup> and assuming an average  $[\alpha/\text{Fe}]$  value of 0.3 (Recio-Blanco 2018), we derive for 1b and 2b a  $[\text{Fe}/\text{H}]$  value lower limit of  $-1.7$  ( $0.03 Z_\odot$ ) and an upper limit of  $-0.7$  ( $0.3 Z_\odot$ ). Their ages at redshift 6 correspond to a formation age of  $\sim 12.8$  Gyr.

Comparing to the observed age–metallicity relation in the Local Group, where the age determination for globular clusters is more robust, we observe that the Sunrise arc YMCs have metallicity ranges that overlap with the old ( $\sim 12$  Gyr) metal-poor branch of globular clusters of the Milky Way and Large Magellanic Cloud (Forbes & Bridges 2010; Narloch et al. 2022).

The derived masses of the YMCs are all above  $10^6 M_\odot$  (Table 3). Even by making the conservative assumption that about 75% of their mass is lost during a Hubble time evolution (Reina-Campos et al. 2018), their masses will still be close to or larger than the characteristic masses of globular cluster populations observed in the local universe (e.g.,  $\sim 2 \times 10^5 M_\odot$ ; Brodie & Strader 2006). We conclude that the YMCs in the Sunrise arc might evolve into metal-poor globular clusters that will likely populate the outskirts of galaxies at redshift zero.

Finally, by simply dividing the total mass in clusters versus the host one, we find that between 1% and 10% of the total stellar mass in the Sunrise galaxy is located in these young star clusters. To understand whether the fractions we report are extreme, we can look at the local universe for a comparison. However, young star cluster formation in the local universe is happening in already-evolved disk galaxies for which the bulk of the mass has been assembled around the cosmic noon. It is therefore more appropriate to look at globular cluster populations. Larsen et al. (2012) reported that the total stellar mass in the metal-poor globular clusters associated with the Milky Way halo is about 2% of the total mass of the halo component. On the opposite extreme end, in the low-mass dwarf spheroidal Fornax, five massive and metal-poor globular clusters constitute about 30%–50% of the total stellar mass in the galaxy at those metallicity ranges. So we conclude that the cluster population detected in the Sunrise arc is well within the expectation of star cluster formation during galaxy assembly.

<sup>37</sup>  $[\text{Fe}/\text{H}] = [\text{M}/\text{H}] - A \times [\alpha/\text{Fe}]$ , where  $A = 0.75$ .

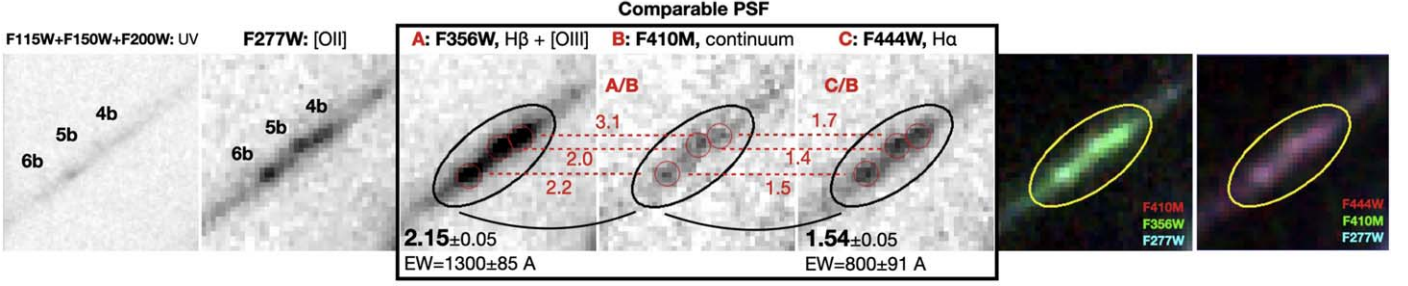


**Figure 6.** Star-forming complex (SFC) at position “b.” From left to right: the stacked image probing the ultraviolet wavelength (1600–2800 Å); F277W, in which knots 4b, 5b, and 6b are identified; and F356W, F410M, and F444W, probing the indicated lines and continuum with the reported flux ratios (image A/B) for each knot (red) and the elliptical aperture (black) corresponding to rest-frame equivalent widths  $EW \simeq 1300$  and  $800$  Å for  $H\beta + [O III]$  and  $H\alpha$  nebular lines, respectively. The rightmost images show the same color images shown in Figure 1.

**Table 3**  
Intrinsic (Source Plane) Physical Properties of the Multiple Image Systems Shown in Figure 1

ID	$M_{2000}$ F150W	$M_{5700}$ F410M	Stellar Mass ( $10^6 M_{\odot}$ )	Age (Myr)	$E(B - V)$	$R_{\text{eff}}$ (pc) [mas]	$\Pi$	$\Sigma_{\text{mass}}$ ( $10^3 M_{\odot} \text{ pc}^{-2}$ )	$\mu_{\text{tot}}$	$\mu_{\text{tang}}$
(1)	(2)	(3)	(4)	(5)	(6)	(7)	(8)	(9)	(10)	(11)
1b	−15.22	−15.54	$7.1^{+1.6}_{-4.6}$	$30^{+0}_{-22}$	$0.00^{+0.10}_{-0.00}$	$1.4^{+0.3}_{-0.7}$ [15]	$314.1^{+297.6}_{-155.8}$	$311.3^{+445.5}_{-158.1}$	$\gtrsim 66$	$\gtrsim 60$
2b	−15.34	−15.41	$3.9^{+0.2}_{-1.3}$	$10^{+0}_{-1}$	$0.10^{+0.00}_{-0.05}$	$6.3^{+1.1}_{-1.3}$ [30]	$8.3^{+3.1}_{-1.9}$	$8.7^{+4.8}_{-2.7}$	$\gtrsim 30$	$\gtrsim 27$
3b <sup>a</sup>	−13.58	−14.26	$1.1^{+8.7}_{-0.5}$	$4^{+36}_{-3}$	$0.25^{+0.20}_{-0.20}$	$6.1^{+12.5}_{-3.6}$ [29]	$1.9^{+15.7}_{-0.9}$	$2.7^{+16.3}_{-2.3}$	$\gtrsim 30$	$\gtrsim 27$
4b <sup>a</sup>	−16.84	−16.91	$10.1^{+11.0}_{-0.2}$	$1^{+3}_{-0}$	$0.15^{+0.15}_{-0.05}$	$24.8^{+62.6}_{-12.3}$ [117]	$0.2^{+0.4}_{-0.1}$	$1.5^{+2.1}_{-0.8}$	$\gtrsim 30$	$\gtrsim 27$
5b <sup>a</sup>	−13.50	−14.51	$3.1^{+10.2}_{-2.0}$	$6^{+74}_{-5}$	$0.40^{+0.25}_{-0.30}$	$4.9^{+10.6}_{-1.7}$ [23]	$6.6^{+62.6}_{-3.3}$	$11.8^{+41.6}_{-9.1}$	$\gtrsim 30$	$\gtrsim 27$
6b	−15.70	−15.83	$3.3^{+3.2}_{-0.8}$	$4^{+2}_{-3}$	$0.15^{+0.05}_{-0.10}$	$8.5^{+2.1}_{-3.0}$ [40]	$2.0^{+2.2}_{-1.1}$	$4.1^{+5.6}_{-2.4}$	$\gtrsim 30$	$\gtrsim 27$
SFCd <sup>b</sup>	−17.64	−17.69	$266^{+234}_{-122}$	$140^{+140}_{-80}$	$0.24^{+11}_{-10}$	$\simeq 200^d$	...	...	18	16
SFCd <sup>c</sup>	−17.64	−17.69	$44 \pm 11$	$11 \pm 2$	...	$\simeq 200^d$	...	...	18	16
SFCd <sup>oo</sup>	−17.64	−17.69	$97 \pm 20$	$130 \pm 35$	...	$\simeq 200^d$	...	...	18	16
TOTd <sup>b</sup>	−17.93	−18.14	$2200^{+3010}_{-1200}$	$201^{+93}_{-108}$	$0.09^{+0.05}_{-0.04}$	$\simeq 1000^d$	...	...	15	13
TOTd <sup>oo</sup>	−17.93	−18.14	$300^{+60}_{-40}$	$185 \pm 50$	...	$\simeq 1000^d$	...	...	15	13

**Notes.** Column (1) lists the IDs of the sources. Columns (2) and (3) report the absolute magnitudes in the rest-frame ultraviolet and optical. Such magnitudes are likely upper limits given the limits on magnification (see column (10)). Columns (4), (5), and (6) show the stellar masses, ages, and  $E(B - V)$  inferred from the SED fitting; the effective radius is listed in column (7), based on the F150W band for 1b, 2b, 6b, and SFC and F277W for nebular knots 3b, 4b, and 5b. Columns (8) and (9) summarize the dynamical age  $\Pi$  and the stellar mass surface density  $\Sigma_{\text{mass}}$ . Lower limits on the total and tangential magnifications are reported in columns (10) and (11), respectively. In the approximation in which  $\mu_{\text{tot}} \simeq \mu_{\text{tang}}$  as in this system, the stellar masses and effective radii scale as  $\mu_{\text{tot}}^{-1}$  and  $\mu_{\text{tang}}^{-1}$ , whereas  $\Pi$  and  $\Sigma_{\text{mass}}$  are directly proportional to  $\mu_{\text{tot}}$ .

<sup>a</sup> Nebular knots.

<sup>b</sup> Prospector-based SED fitting with flexible SFHs. Quoted ages are mass-weighted.

<sup>c</sup> BAGPIPES-based SED fitting with one (o) and two (oo) components of constant star formation. Quoted ages are mass-weighted.

<sup>d</sup> The size refers to the extent of the region (not the effective radius). The reported error bars do not include uncertainties on the magnifications, which are considered lower limits in this work (see Appendix A).

## 5.2. High Ionizing Photon Production Efficiency

A prominent feature of the Sunrise galaxy that clearly emerges by means of our JWST/NIRCam imaging is the multiple-image star-forming complex SFC shown in Figures 1 and 2. In such a region, which extends about 200 pc in the source plane, significant enhanced flux is detected in the F356W band if compared to the continuum probed by the F410M filter (corresponding to  $\simeq 5.9 \times 10^{-17} \text{ erg s}^{-1} \text{ cm}^{-2}$ ), potentially implying rest-frame equivalent widths of the group of lines  $H\beta + [O III]$  of  $\simeq 1300$  Å (Figures 1 and 4). The same region also shows a clear excess in F444W (producing a flux of  $\simeq 2.3 \times 10^{-17} \text{ erg s}^{-1} \text{ cm}^{-2}$ ) ascribed to the strong  $H\alpha$  line with a rest-frame equivalent width  $\simeq 800$  Å. Figure 6 shows the zoomed SFC at position “b” (the most magnified one), in which knots 4b, 5b, and 6b are clearly identified, along with their significant flux contrast imprinted in the JWST/NIRCam

photometry (Figure 5), overall associated with large rest-frame equivalent widths. As discussed above, SFC hosts very young stellar clusters ( $\lesssim 10$  Myr; 4b, 5b, and 6b, associated with a large specific SFR,  $s\text{SFR} \simeq 100 \text{ Gyr}^{-1}$ ), in which O-type stars produce a vigorous ionization field and strong lines boosting the photometry as observed (the fraction of ionizing photons converted into lines is unknown; we assume  $>50\%$ ).

The SED fitting of SFC is shown in Figure 5, and the properties are reported in Table 3. The large sSFR and equivalent widths of the optical nebular lines also imply a large ionizing photon production efficiency  $\xi_{\text{ion}}$  according to the positive correlation with the [O III] line strength (e.g., Chevallard et al. 2018; Emami et al. 2020; Nakajima et al. 2020). Precise line fluxes will be measured with JWST/NIRSpec; however,  $\xi_{\text{ion}}$  can also be estimated with the present data. The  $H\alpha$  luminosity associated with the flux derived above and combined with the ultraviolet

luminosity at  $1500 \text{ \AA}$  inferred from the F115W band provides  $\log(\xi_{\text{ion}} [\text{Hz erg}^{-1}]) \sim 25.7$  without any dust correction. Corrections for dust attenuation or leakage of ionizing photons could decrease or increase  $\xi_{\text{ion}}$ , respectively. Such a crude value is in line with previous studies at similar faint luminosity regimes and  $\text{H}\alpha$  equivalent widths (e.g., Maseda et al. 2020; Nakajima et al. 2020, 2022) and the values reported recently by Matthee et al. (2022) derived with JWST/NIRCam slitless spectroscopy at  $z \sim 5\text{--}7$ . While the direct measure of escaping ionizing radiation is not possible at the redshift of *Sunrise*, it is worth noting that the presence of multiple star clusters (young and relatively evolved) implies that the *Sunrise* galaxy was subjected to a progressive injection of energy and stellar feedback in the ISM (e.g., 1b and 2b were active a few tens of megayears before SFC) eventually favoring the construction of ionized channels and the escape of ionizing radiation into the intergalactic medium. A direct similar example has been observed in the *Sunburst* Lyman continuum galaxy at  $z = 2.37$  (Vanzella et al. 2022a; see also Rivera-Thorsen et al. 2019; Mainali et al. 2022). Also, in local starburst galaxies, such conditions have recently been observed in great detail (e.g., Bik et al. 2018; Sirressi et al. 2022). Such an iterated star cluster formation would make the escape of ionizing radiation an intermittent process, which temporally correlates with the bursty star-forming phases (e.g., Wise et al. 2014; Trebitsch et al. 2017).

## 6. Concluding Remarks

The optical rest-frame coverage at  $z \simeq 6.0$  (up to  $7000 \text{ \AA}$ ) and the enhanced angular resolution (three times better than HST in the *H* band) provided by JWST/NIRCam have allowed us to derive the stellar masses, ages, and dust attenuation and refine the sizes of the compact sources hosted in the *Sunrise* arc, which we conclude are massive stellar clusters (see Table 3). It is worth noting that if JWST/NIRSpec confirms the presence of emission lines in these systems at a much higher spectral resolution, JWST/NIRCam imaging still provides a continuous 2D view with a remarkably high spatial contrast (down to scales of a few parsecs along the tangential stretch) of such prominent lines along the arc. There are three main results from our study.

1. *Proto-globular clusters in the reionization era.* The inferred properties of clusters 1b and 2b (i.e., effective radii  $< 5 \text{ pc}$ , old dynamical ages  $\Pi \gg 1$ , and stellar mass surface densities well above  $1000 M_{\odot} \text{ pc}^{-2}$ ) qualify them as bound star clusters. If they survive until the present day, these systems will appear as a few  $\sim 10^6 M_{\odot}$ ,  $\simeq 12.5\text{--}13 \text{ Gyr}$  old, likely metal-poor globular clusters. Source 6b is also massive but still very young. It is part of a larger star-forming complex (SFC;  $\sim 200 \text{ pc}$  size), which includes two additional nebular knots plausibly hosting relatively dense and UV dust-attenuated star clusters. Such systems might host GCPs caught in the act of their initial formation phase.
2. *Ionization.* The star-forming complex “SFC” hosts very young stellar populations (age  $< 5 \text{ Myr}$ ) and is likely located in star clusters sharing the same natal region (of  $\sim 200 \text{ pc}$  size). The SFC also dominates the nebular emission line budget of the *Sunrise* galaxy. In particular, the ionizing photon production efficiency we estimate for SFC is remarkably high,  $\log(\xi_{\text{ion}} [\text{Hz erg}^{-1}]) \sim 25.7$ , which is fully in line with the large rest-frame equivalent widths of

the optical nebular lines inferred from the photometric discontinuities ( $[\text{O III}]$  rest-frame equivalent widths  $\gtrsim 1000 \text{ \AA}$ ). The high occurrence of such prominent optical nebular emission lines observed at  $z > 6$  (e.g., Boyett et al. 2022; Matthee et al. 2022) and the connection with bursty events driven by very young stellar clusters as probed in lensed galaxies such as *Sunrise* (and similarly by the *Sunburst* arc; Vanzella et al. 2022a) suggest that stellar cluster formation activity was significant during reionization.

3. *Host galaxy.* Mass-weighted age estimates suggest that the stellar mass of the *Sunrise* arc has been assembled in the last few hundred megayears. Overall, these six YMCs constitute less than 10% of the total mass of the host galaxy. When focusing on the recent SFH, we estimate that the stellar mass in clusters is an important fraction of the recently formed stellar mass in the galaxy (lower limits to the CFE are in the range of 10%–30%). We conclude that the cluster formation currently taking place in the *Sunrise* arc is an important contribution to the stellar mass buildup and galactic stellar feedback.

This work is based on observations made with the NASA/ESA/CSA James Webb Space Telescope (JWST) and Hubble Space Telescope (HST). These observations are associated with JWST GO program 2282 and HST GO programs 14096, 15842, and 16668. The data (doi:10.17909/cqfq-5n80) were obtained from the Mikulski Archive for Space Telescopes (MAST) at the Space Telescope Science Institute (STScI), which is operated by the Association of Universities for Research in Astronomy (AURA), Inc., under NASA contract NAS 5-03127 for JWST. We acknowledge financial support from NASA through grant JWST-GO-02282.

We thank the anonymous referee for the constructive comments. A.A. acknowledges support from the Swedish Research Council (Vetenskapsrådet project grant 2021-05559). A.A. and A.C. thank M. Messa for sharing an earlier version of his software. E.V. acknowledges financial support through grants PRIN-MIUR 2017WSCC32 and 2020SKSTHZ and INAF “main-stream” grants 1.05.01.86.20 and 1.05.01.86.31. We acknowledge support from INAF GO grant 2022, “The revolution is around the corner: JWST will probe globular cluster precursors and Population III stellar clusters at cosmic dawn” (PI: Vanzella). J.M.D. acknowledges the support of projects PGC2018-101814-B-100 and MDM-2017-0765. M.B. acknowledges support from the Slovenian national research agency ARRS through grant N1-0238. P.D. acknowledges support from NWO grant 016.VIDI.189.162 (“ODIN”) and the European Commission’s and University of Groningen’s CO-FUND Rosalind Franklin program. M.O. acknowledges support from JSPS KAKENHI grant Nos. JP22H01260, JP20H05856, and JP20H00181. S.F. acknowledges support from NASA through NASA Hubble Fellowship grant HST-HF2-51505.001-A awarded by the Space Telescope Science Institute, which is operated by the Association of Universities for Research in Astronomy, Inc., under NASA contract NAS5-26555. B.W. acknowledges support from NASA under award No. 80GSFC21M0002. L.J.F. and A.Z. acknowledge support by grant No. 2020750 from the United States–Israel Binational Science Foundation (BSF), grant No. 2109066 from the United States National Science Foundation (NSF), and the Ministry of Science & Technology, Israel. E.V. thanks the colleague Antonio Sollima for inspiring discussions on local stellar

clusters; Antonio, unfortunately, passed away prematurely at the age of 43, during the acceptance of this work.

*Facility:* This work is based on observations made with the NASA/ESA/CSA James Webb Space Telescope (JWST) and Hubble Space Telescope (HST).

### Appendix A Photometric Redshift of the Sunrise Arc

The extended wavelength coverage provided by JWST/NIRCam imaging (up to 7000 Å rest frame) allows us to properly highlight the presence of underlying prominent optical nebular emission lines. The color images reported in Figure 1 clearly show the enhanced flux produced by Hβ+[O III] in the F356W band, while the F277W (blue channel) and

F410M (red channel) bands probe the underlying stellar continuum at 3800 and 5700 Å rest frame without intercepting any significant emission lines, respectively.<sup>38</sup> Similarly, the same figure shows the Hα boosting in F444W (red channel). It is also worth noting that this new JWST/NIRCam rest-frame optical view of the Sunrise arc significantly improves the photometric redshift of the arc. In fact, the absence of the above lines in the medium filter F410M implies a minimum and maximum redshift of ~5.5 and ~6.7, which, coupled with the >2 mag drop at λ < 0.9 μm, places the arc at  $z_{\text{phot}} = 5.9^{+0.3}_{-0.2}$  without lower-redshift solutions. The photometry of the full arc used in the fit is obtained by combining all of the segments as described in Figure 2. The redshift probability distribution is shown in Figure 7.

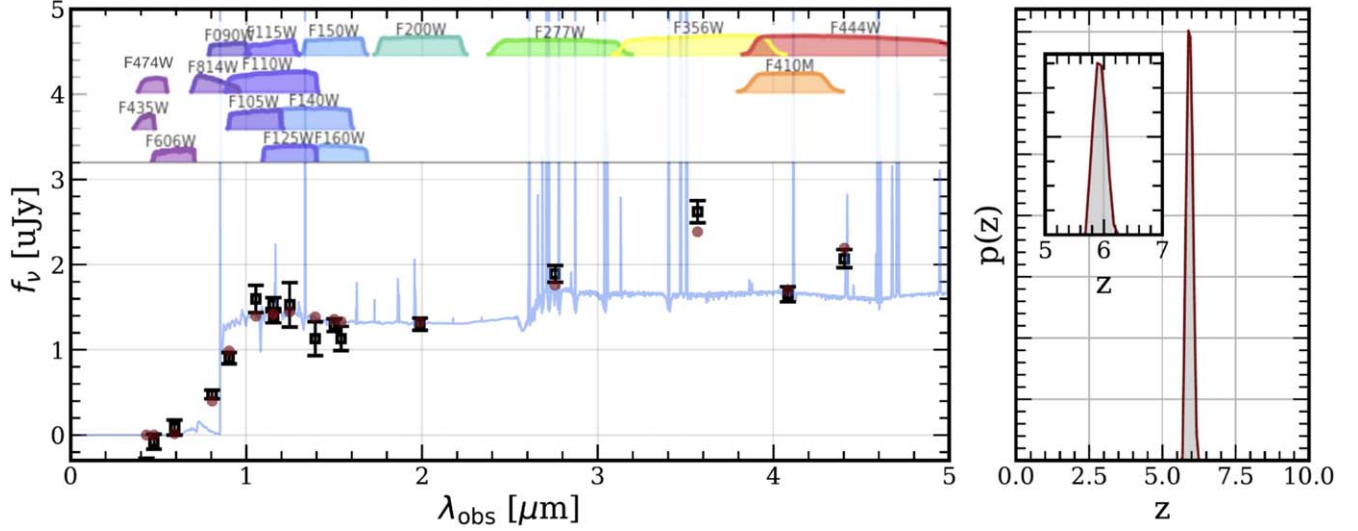


**Figure 7.** Left: photometry of the full Sunrise arc (black squares with error bars) and EAZY SED fit (blue spectrum with red circles for model fluxes). We sum the PSF-matched isophotal photometry in all detected segments except 6c, which is blended with the interloper (a likely galaxy cluster member; see Figure 2). Right: redshift probability distribution  $z = 5.9^{+0.3}_{-0.2}$  (95% CL).

<sup>38</sup> It is worth noting that the F277W band includes the [O II] emission, whose effect, however, appears not to be significant in the present case.

## Appendix B Magnifications of the Star-forming Regions

Figure 8 shows the JWST/NIRCam color image of the compact sources detected in the ultraviolet (1600–2800 Å) and reported in Table 3.

Lens models based on HST imaging were presented and made publicly available by Welch et al. (2022a). Significant updates will be possible based on upcoming VLT/MUSE spectroscopic observations (PI: G. B. Caminha). In this work, we make minor updates to lens models derived using three methods: WSLAP+ (Diego et al. 2005, 2007), Lenstool (Jullo et al. 2007; Jullo & Kneib 2009), and GLAFIC (Oguri 2010, 2021). The primary magnification estimates presented here are from WSLAP+. This model produces a critical curve that bends away from the arc after image 6c, resulting in magnifications for images 6d, 2d, and 1d lower than seen in other models. We adopt this as our baseline model to give the most conservative magnification estimate while the lens models are continuing to be refined. For comparison, we also show the preliminary updated Lenstool model, which produces critical curves that more tightly trace the arc (see red curve in Figure 8), leading to higher predicted magnifications. This configuration introduces additional uncertainty on the magnification estimates; thus, we adopt the lower-magnification model to be conservative.

In this work, we adopt a similar approach described in, e.g., Vanzella et al. (2017) to estimate the values of amplification for the most magnified knots (labeled as “b” in Figure 8). Specifically, the magnifications of the least magnified images (group d, which is affected by modest uncertainties of <10%) are rescaled to b locations according to the measured flux ratios between d and b pairs. The flux ratios were inferred from the stacked image F115W+F150W+F200W. Unlike in the case of gravitationally lensed quasars, for strongly lensed compact stellar regions of sizes greater than 0.5 pc, magnification ratios are unaffected by microlensing effects and hence are reliable proxies for the magnification ratio. Figure 8 shows the locations of knots 1b and d, 2b and d, and 6b and d and the inferred flux ratios measured within circular apertures of a fixed diameter of  $0''.2$ . The three knots (1, 2, and 6) bracket the entire portion of the Sunrise arc we are analyzing in this work. It is worth noting that the physical regions probed by using fixed aperture sizes are different among multiple images because of the underlying different amplification. In particular, the larger physical regions probed by the apertures in group d (with regard to group b) imply that the flux ratios are lower limits. Consequently, the rescaled values of  $\mu_{\text{tot}}$  at b reported in Figure 8 and Table 3 are likely lower limits (after adopting  $\mu$  values in d) and show values higher than 30. As an additional

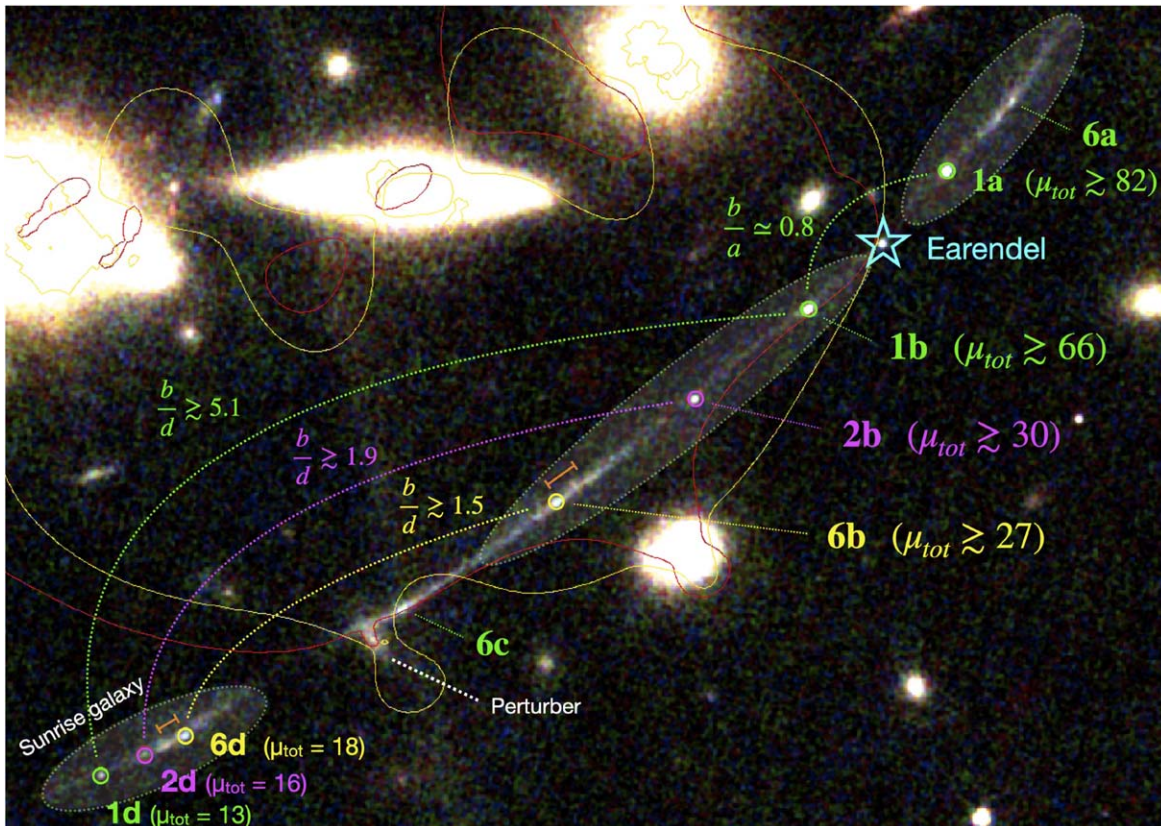


**Figure 8.** The JWST/NIRCam color composites of the Sunrise arc with the knots detected in the ultraviolet wavelengths indicated: 1 (green), 2 (magenta), and 6 (yellow); see Table 3. Multiple image pairs are indicated with dotted lines adopting the same color coding. The flux ratios ( $b/d$ ) are also reported for each pair. The amplifications  $\mu_{\text{tot}}$  in b are indicated as likely lower limits (see text for details). The yellow and red contours show the critical curves for the current lens models based on JWST imaging (and will be presented in more detail in a forthcoming paper). While the configurations presented by the red curve trace the arc more tightly, the model presenting the yellow curve represents our most realistic and conservative amplification. The separations between knots in the SFC are indicated with orange segments at positions d and b, and their ratio of  $\approx 1.6$  ( $b/d$ ) is in line with the expectation from the flux ratio reported. The three transparent white ellipses mark the same three multiple regions subjected to different magnifications. The region indicated with 6c (which is the same star-forming region observed on the other multiple segments, 6a, 6b, and 6d) is associated with the perturber that bends the critical lines and amplifies a subcomponent of the Sunrise galaxy (a better analysis of that region will require spectroscopic confirmation and additional physical properties of the interloper and will be part of the work in preparation).

test, the orange segments show the separations between 4b and 6b and between 4d and 6d whose ratio  $b/d \simeq 1.6$  (associated with the tangential magnification ratio) is consistent with the flux ratio reported (related to the total magnification ratio).

Conservatively, for all knots listed in Table 3, we adopt  $\mu_{\text{tot}} = 30$ , except for 1b, for which we adopt  $\mu_{\text{tot}} \gtrsim 66$ . The corresponding tangential magnification  $\mu_{\text{tang}}$  along the arc is derived by dividing the above  $\mu_{\text{tot}}$  values by the radial magnification, which in this case is quite stable along the full arc with a median value of  $\simeq 1.1$ . The magnifications of group d are based on a new lens model that is based on JWST/NIRCam identifications of the multiple images and will be presented in a forthcoming work. Table 3 reports such lower limits.

### ORCID iDs

Eros Vanzella  <https://orcid.org/0000-0002-5057-135X>  
 Adélaïde Claeysens  <https://orcid.org/0000-0001-7940-1816>  
 Brian Welch  <https://orcid.org/0000-0003-1815-0114>  
 Angela Adamo  <https://orcid.org/0000-0002-8192-8091>  
 Dan Coe  <https://orcid.org/0000-0001-7410-7669>  
 Jose M. Diego  <https://orcid.org/0000-0001-9065-3926>  
 Guillaume Mahler  <https://orcid.org/0000-0003-3266-2001>  
 Gourav Khullar  <https://orcid.org/0000-0002-3475-7648>  
 Vasily Kokorev  <https://orcid.org/0000-0002-5588-9156>  
 Masamune Oguri  <https://orcid.org/0000-0003-3484-399X>  
 Swara Ravindranath  <https://orcid.org/0000-0002-5269-6527>  
 Lukas J. Furtak  <https://orcid.org/0000-0001-6278-032X>  
 Tiger Yu-Yang Hsiao  <https://orcid.org/0000-0003-4512-8705>  
 Abdurro'uf  <https://orcid.org/0000-0002-5258-8761>  
 Nir Mandelker  <https://orcid.org/0000-0001-8057-5880>  
 Gabriel Brammer  <https://orcid.org/0000-0003-2680-005X>  
 Larry D. Bradley  <https://orcid.org/0000-0002-7908-9284>  
 Maruša Bradač  <https://orcid.org/0000-0001-5984-0395>  
 Christopher J. Conselice  <https://orcid.org/0000-0003-1949-7638>  
 Pratika Dayal  <https://orcid.org/0000-0001-8460-1564>  
 Mario Nonino  <https://orcid.org/0000-0001-6342-9662>  
 Felipe Andrade-Santos  <https://orcid.org/0000-0002-8144-9285>  
 Rogier A. Windhorst  <https://orcid.org/0000-0001-8156-6281>  
 Nor Pirzkal  <https://orcid.org/0000-0003-3382-5941>  
 Keren Sharon  <https://orcid.org/0000-0002-7559-0864>  
 S. E. de Mink  <https://orcid.org/0000-0001-9336-2825>  
 Seiji Fujimoto  <https://orcid.org/0000-0001-7201-5066>  
 Adi Zitrin  <https://orcid.org/0000-0002-0350-4488>  
 Jan J. Eldridge  <https://orcid.org/0000-0002-1722-6343>  
 Colin Norman  <https://orcid.org/0000-0002-5222-5717>

### References

- Adamo, A., Hollyhead, K., Messa, M., et al. 2020b, *MNRAS*, 499, 3267  
 Adamo, A., Östlin, G., & Zackrisson, E. 2011, *MNRAS*, 417, 1904  
 Adamo, A., Zackrisson, E., Östlin, G., & Hayes, M. 2010, *ApJ*, 725, 1620  
 Adamo, A., Ryon, J. E., Messa, M., et al. 2017, *ApJ*, 841, 131  
 Adamo, A., Zeidler, P., Kruijssen, J. M. D., et al. 2020a, *SSRv*, 216, 69  
 Asplund, M., Grevesse, N., Sauval, A. J., & Scott, P. 2009, *ARA&A*, 47, 481  
 Barbary, K. 2016, *JOSS*, 1, 58  
 Bergamini, P., Grillo, C., Rosati, P., et al. 2022, arXiv:2208.14020  
 Bik, A., Östlin, G., Menacho, V., et al. 2018, *A&A*, 619, A131  
 Bouwens, R. J., Illingworth, G. D., van Dokkum, P. G., et al. 2021, *AJ*, 162, 255  
 Bouwens, R. J., Illingworth, G. D., van Dokkum, P. G., et al. 2022, *ApJ*, 927, 81  
 Boyett, K. N. K., Stark, D. P., Bunker, A. J., Tang, M., & Maseda, M. V. 2022, *MNRAS*, 513, 4451  
 Bradley, L. D., Coe, D., Brammer, G., et al. 2022, arXiv:2210.01777  
 Brammer, G., Strait, V., Matharu, J., & Momcheva, I. 2022, grizli, v1.5.0, Zenodo, doi:10.5281/zenodo.6672538  
 Brodie, J. P., & Strader, J. 2006, *ARA&A*, 44, 193  
 Brown, G., & Gnedin, O. Y. 2021, *MNRAS*, 508, 5935  
 Bruzual, G., & Charlot, S. 2003, *MNRAS*, 344, 1000  
 Calzetti, D., Armus, L., Bohlin, R. C., et al. 2000, *ApJ*, 533, 682  
 Carnall, A. C., McLure, R. J., Dunlop, J. S., & Dave, R. 2018, *MNRAS*, 480, 4379  
 Chabrier, G. 2003, *PASP*, 115, 763  
 Chevillard, J., Charlot, S., Senchyna, P., et al. 2018, *MNRAS*, 479, 3264  
 Choi, J., Dotter, A., Conroy, C., et al. 2016, *ApJ*, 823, 102  
 Claeysens, A., Adamo, A., Richard, J., et al. 2023, *MNRAS*, 520, 2180  
 Coe, D., Salmon, B., Bradac, M., et al. 2019, *ApJ*, 884, 85  
 Conroy, C., & Gunn, J. E. 2010, *ApJ*, 712, 833  
 Diego, J. M., Protopapas, P., Sandvik, H. B., & Tegmark, M. 2005, *MNRAS*, 360, 477  
 Diego, J. M., Tegmark, M., Protopapas, P., & Sandvik, H. B. 2007, *MNRAS*, 375, 958  
 Ellis, R., Santos, M. R., Kneib, J.-P., & Kuijken, K. 2001, *ApJL*, 560, L119  
 Elmegreen, D. M., Elmegreen, B. G., Whitmore, B. C., et al. 2021, *ApJ*, 908, 121  
 Emami, N., Siana, B., Alavi, A., et al. 2020, *ApJ*, 895, 116  
 Falcón-Barroso, J., Sánchez-Blázquez, P., Vazdekis, A., et al. 2011, *A&A*, 532, A95  
 Ferland, G. J., Chatzikos, M., Guzmán, F., et al. 2017, *RMxAA*, 53, 385  
 Ferland, G. J., Korista, K. T., Verner, D. A., et al. 1998, *PASP*, 110, 761  
 Ferland, G. J., Porter, R. L., van Hoof, P. A. M., et al. 2013, *RMxAA*, 49, 137  
 Forbes, D. A., & Bridges, T. 2010, *MNRAS*, 404, 1203  
 Gaia Collaboration, Brown, A. G. A., Vallenari, A., et al. 2021, *A&A*, 649, A1  
 Gieles, M., & Portegies Zwart, S. F. 2011, *MNRAS*, 410, L6  
 Göteborg, Y., de Mink, S. E., Groh, J. H., et al. 2018, *A&A*, 615, A78  
 Göteborg, Y., de Mink, S. E., Groh, J. H., Leitherer, C., & Norman, C. 2019, *A&A*, 629, A134  
 Heckman, T. M., Borthakur, S., Overzier, R., et al. 2011, *ApJ*, 730, 5  
 Herenz, E. C., Hayes, M., Papaderos, P., et al. 2017, *A&A*, 606, L11  
 Hsiao, T., Coe, D., & Abdurro'uf 2022, arXiv:2210.14123  
 James, B. L., Auger, M., Aloisi, A., Calzetti, D., & Kewley, L. 2016, *ApJ*, 816, 40  
 Johnson, B. D., Leja, J., Conroy, C., & Speagle, J. S. 2021, *ApJS*, 254, 22  
 Johnson, T. L., Rigby, J. R., Sharon, K., et al. 2017, *ApJL*, 843, L21  
 Jullo, E., & Kneib, J.-P. 2009, *MNRAS*, 395, 1319  
 Jullo, E., Kneib, J.-P., Limousin, M., et al. 2007, *NJPh*, 9, 447  
 Khullar, G., Gozman, K., Lin, J. J., et al. 2021, *ApJ*, 906, 107  
 Kokorev, V., Brammer, G., Fujimoto, S., et al. 2022, *ApJ*, 263, 38  
 Kriek, M., & Conroy, C. 2013, *ApJL*, 775, L16  
 Kroupa, P. 2001, *MNRAS*, 322, 231  
 Kroupa, P. 2002, *Sci*, 295, 82  
 Krumholz, M. R., McKee, C. F., & Bland-Hawthorn, J. 2019, *ARA&A*, 57, 227  
 Larsen, S. S., Strader, J., & Brodie, J. P. 2012, *A&A*, 544, L14  
 Leitherer, C., Ekström, S., Meynet, G., et al. 2014, *ApJS*, 212, 14  
 Leja, J., Carnall, A. C., Johnson, B. D., Conroy, C., & Speagle, J. S. 2019, *ApJ*, 876, 3  
 Livermore, R. C., Finkelstein, S. L., & Lotz, J. M. 2017, *ApJ*, 835, 113  
 Mainali, R., Rigby, J. R., Chisholm, J., et al. 2022, *ApJ*, 940, 160  
 Maseda, M. V., Bacon, R., Lam, D., et al. 2020, *MNRAS*, 493, 5120  
 Matthee, J., Mackenzie, R., Simcoe, R. A., et al. 2022, arXiv:2211.08255  
 Messa, M., Dessauges-Zavadsky, M., Richard, J., et al. 2022, *MNRAS*, 516, 2420  
 Meštrić, U., Vanzella, E., Zanella, A., et al. 2022, *MNRAS*, 516, 3532  
 Micheva, G., Oey, M. S., Jaskot, A. E., & James, B. L. 2017, *ApJ*, 845, 165  
 Mowla, L., Iyer, K. G., Desprez, G., et al. 2022, *ApJL*, 937, L35  
 Nakajima, K., Ellis, R. S., Robertson, B. E., Tang, M., & Stark, D. P. 2020, *ApJ*, 889, 161  
 Nakajima, K., Ouchi, M., Xu, Y., et al. 2022, *ApJS*, 262, 3  
 Narloch, W., Pietrzyński, G., Gieren, W., et al. 2022, *A&A*, 666, A80  
 Norris, M. A., Kannappan, S. J., Forbes, D. A., et al. 2014, *MNRAS*, 443, 1151  
 Oguri, M. 2010, *PASJ*, 62, 1017

- Oguri, M. 2021, *PASP*, 133, 074504
- Oke, J. B., & Gunn, J. E. 1983, *ApJ*, 266, 713
- Östlin, G., Cumming, R. J., & Bergvall, N. 2007, *A&A*, 461, 471
- Plazas, A. A., Meneghetti, M., Maturi, M., & Rhodes, J. 2019, *MNRAS*, 482, 2823
- Pontoppidan, K., Blome, C., Braun, H., et al. 2022, *ApJL*, 936, L14
- Recio-Blanco, A. 2018, *A&A*, 620, A194
- Reina-Campos, M., Kruijssen, J. M. D., Pfeffer, J., Bastian, N., & Crain, R. A. 2018, *MNRAS*, 481, 2851
- Rigby, J. R., Johnson, T. L., Sharon, K., et al. 2017, *ApJ*, 843, 79
- Rivera-Thorsen, T. E., Dahle, H., Chisholm, J., et al. 2019, *Sci*, 366, 738
- Ryon, J. E., Gallagher, J. S., Smith, L. J., et al. 2017, *ApJ*, 841, 92
- Salim, S., Boquien, M., & Lee, J. C. 2018, *ApJ*, 859, 11
- Salmon, B., Coe, D., Bradley, L., et al. 2020, *ApJ*, 889, 189
- Sharon, K., Mahler, G., Rivera-Thorsen, T. E., et al. 2022, *ApJ*, 941, 203
- Sirressi, M., Adamo, A., Hayes, M., et al. 2022, *MNRAS*, 510, 4819
- Stanway, E. R., & Eldridge, J. J. 2018, *MNRAS*, 479, 75
- Sukay, E., Khullar, G., Gladders, M. D., et al. 2022, *ApJ*, 940, 42
- Trebitsch, M., Blaizot, J., Rosdahl, J., Devriendt, J., & Slyz, A. 2017, *MNRAS*, 470, 224
- Treu, T., Roberts-Borsani, G., Bradac, M., et al. 2022, *ApJ*, 935, 110
- Vanzella, E., Calura, F., Meneghetti, M., et al. 2017, *MNRAS*, 467, 4304
- Vanzella, E., Calura, F., Meneghetti, M., et al. 2019, *MNRAS*, 483, 3618
- Vanzella, E., Caminha, G. B., Rosati, P., et al. 2021, *A&A*, 646, A57
- Vanzella, E., Castellano, M., Bergamini, P., et al. 2022a, *A&A*, 659, A2
- Vanzella, E., Castellano, M., Bergamini, P., et al. 2022b, *ApJL*, 940, L53
- Vazdekis, A., Koleva, M., Ricciardelli, E., Röck, B., & Falcon-Barroso, J. 2016, *MNRAS*, 463, 3409
- Vazdekis, A., Coelho, P., Cassisi, S., et al. 2015, *MNRAS*, 449, 1177
- Welch, B., Coe, D., Zitrin, A., et al. 2023, *ApJ*, 943, 2
- Welch, B., Coe, D., Diego, J. M., et al. 2022a, *Natur*, 603, 815
- Welch, B., Coe, D., Zackrisson, E., et al. 2022b, *ApJL*, 940, L1
- Wen, Z. L., & Han, J. L. 2015, *ApJ*, 807, 178
- Wen, Z. L., Han, J. L., & Liu, F. S. 2012, *ApJS*, 199, 34
- Wise, J. H., Demchenko, V. G., Halicek, M. T., et al. 2014, *MNRAS*, 442, 2560
- Wofford, A., Charlot, S., Bruzual, G., et al. 2016, *MNRAS*, 457, 4296
- Xiao, L., Galbany, L., Eldridge, J. J., & Stanway, E. R. 2019, *MNRAS*, 482, 384
- Xiao, L., Stanway, E. R., & Eldridge, J. J. 2018, *MNRAS*, 477, 904
- Zackrisson, E., Rydberg, C.-E., Schaerer, D., Östlin, G., & Tuli, M. 2011, *ApJ*, 740, 13